Experimental benchmark of pseudo-Hermitian qubit sensing via Naimark dilation

Yue Zhai,[1,2,3] Chao Wei,[1,2,3] Junda Song,[1,2,3] Kada Yang,[1,2,3] Feng Xu,[1,2] Yuquan Xiang,[1,2] Bowen Shao,[1,2] Qingshan Xu,[2] and Tao Xin[2,*]

[1] *Shenzhen Institute for Quantum Science and Engineering, Southern University of Science and Technology, Shenzhen 518055, China*
[2] *International Quantum Academy, Shenzhen 518048, China*
[3] *Shenzhen Key Laboratory of Quantum Science and Engineering, Southern University of Science and Technology, Shenzhen 518055, China*

(Dated: August 1, 2026)

Non-Hermitian dynamics can sharply amplify the response of a quantum sensor near eigenstate coalescence, but whether this amplification yields a genuine metrological gain depends on how the non-unitary evolution is physically realised and how its resources are counted. We address this question experimentally by implementing the pseudo-Hermitian qubit sensing protocol of Chu *et al.* [Phys. Rev. Lett. 124, 020501 (2020)] on a two-qubit nuclear magnetic resonance processor via Naimark dilation. Because both the postselected signal and the full two-qubit probability are obtained from a single set of population measurements, the enhanced response and its postselection cost are accessed within the same experiment. We observe the characteristic steep response of the postselected branch, whereas the sensitivity extracted from the absolute two-qubit probability does not surpass the Ramsey benchmark for the same sensor encoding, consistent with the theoretical resource bound derived by Ding *et al.* [Phys. Rev. Lett. 131, 160801 (2023)] for the corresponding dilation scheme. The experiment complements the recent photonic implementation of the direct non-unitary route and provides an experimental benchmark of the Hermitian-dilation route with explicit resource accounting.

PACS numbers: 03.65.Yz, 03.67.Ac, 06.20.-f, 42.50.Dv
Keywords: non-Hermitian sensing; pseudo-Hermitian qubit; Naimark dilation; postselection; Nuclear Magnetic Resonance; quantum metrology

I. INTRODUCTION

Quantum metrology aims to estimate physical parameters at the ultimate precision allowed by quantum mechanics, exploiting coherence and correlations to approach the quantum Cramér–Rao bound [1–8]. In parallel, non-Hermitian Hamiltonians have become a powerful language for open, dissipative, and gain–loss systems, where parity–time ($\mathcal{PT}$) symmetry and pseudo-Hermiticity can guarantee a real spectrum [9–12], opening a broad field of non-Hermitian physics [13–18]. A hallmark of these systems is the exceptional point (EP), where eigenvalues and eigenvectors coalesce simultaneously [19, 20]. Near an EP, the response of the system to weak perturbations is parametrically large, which has motivated extensive EP-based sensing proposals and demonstrations in microcavities, ring-laser gyroscopes, accelerometers, and quantum platforms [21–33].

Whether this enhanced response translates into a genuine improvement of estimation precision, however, remains under debate [34–40], because eigenvector self-orthogonality at an EP, often quantified by a diverging Petermann factor, can amplify noise and offset the spectral gain when the signal-to-noise ratio is evaluated. A different mechanism was proposed by Chu *et al.* [41], who showed that a single-qubit pseudo-Hermitian Hamiltonian, implemented as a postselected branch of a two-qubit Hermitian dilation, gives a conditional signal whose susceptibility diverges near a point of eigenstate coalescence without the eigenvalue gap closing. The mechanism therefore does not rely on an exceptional point and can instead be realised by coherent unitary control of an enlarged quantum system, without implementing non-unitary evolution directly.

A subsequent quantum-information analysis by Ding *et al.* established a fundamental limit [42, 43], namely that, once the postselection success probability is treated as a physical resource, the postselected branch cannot outperform a fully Hermitian sensor in quantum Fisher information (QFI). On the experimental side, Xiao *et al.* recently demonstrated non-Hermitian sensing without exceptional points in a photonic interferometer with polarisation-dependent loss [44], validating the single-qubit non-Hermitian dynamics on an inherently open platform. What is still missing is an experimental test of the dilation route, in which both the conditional enhancement and the postselection cost predicted by Refs. [41, 42] are measured together on the same device.

In this work, we implement the Naimark-dilated pseudo-Hermitian sensing protocol on a two-qubit nuclear magnetic resonance (NMR) processor [45–47]. The native scalar coupling realises the Hermitian dilation, while a single set of population measurements at each λ yields the conditional signal, the absolute joint probability, and the postselection success probability. We observe the steep conditional response characteristic of pseudo-

* xintao@iqasz.cn

Hermitian sensing as a peak of $S(\lambda)$ at the eigenstate-coalescence point. The sensitivity $\delta\lambda_{P_{00}}$ extracted from the absolute joint probability, rather than from the postselected ratio, stays above the optimal Ramsey benchmark within the reliable working window, consistent with the theoretical analysis of Ref. [42] for this dilation protocol. The present experiment thus complements the photonic implementation of non-Hermitian sensing without exceptional points on a lossy single-qubit platform reported in Ref. [44]. That work realises the non-unitary dynamics directly, whereas our experiment implements the Naimark-dilated Hermitian route and measures the postselection cost.

The paper is organised as follows. Section II presents the pseudo-Hermitian sensing model, its two-qubit Naimark dilation, and the sensitivity bounds used in the resource comparison. Section III describes the NMR implementation and measurement procedure. Section IV reports the measured response and its comparison with the Ramsey reference. Section V discusses the relation to direct non-Hermitian implementations and the main experimental limitations, and Sec. VI concludes the paper.

II. MODEL AND RESOURCE ACCOUNTING

We follow the pseudo-Hermitian qubit sensing protocol of Ref. [41] and implement its Naimark-dilated two-qubit realisation in an NMR processor. The laboratory dynamics is Hermitian on a two-qubit Hilbert space consisting of a sensor qubit s and an ancilla qubit a, while the pseudo-Hermitian single-qubit sensor is the effective description of one branch of that evolution, obtained by postselecting the ancilla outcome. The parameter to be estimated, λ, is encoded as a transverse perturbation on the sensor qubit, equivalently as an offset $b_\lambda = b + \lambda$ in the dilated Hamiltonian defined below, and a Ramsey sequence in which λ accumulates as a dynamical phase on the same sensor qubit provides the Hermitian benchmark used throughout.

A. Effective pseudo-Hermitian sensor

The effective branch [bottom row of Fig. 1(a)] is governed by the single-qubit Hamiltonian of Ref. [41],

$$H_s(E,\delta) = E\begin{pmatrix} 0 & \delta^{-1} \\ \delta & 0 \end{pmatrix}. \tag{1}$$

For $\delta \neq 1$ the off-diagonal elements are unequal, and H_s is non-Hermitian. It belongs nevertheless to the class of pseudo-Hermitian operators [11, 12], since a Hermitian invertible operator η exists with $\eta H_s = H_s^\dagger \eta$, and the spectrum is real, $\pm E$, for all $\delta > 0$. The right eigenstates $|\phi_\pm\rangle \propto |0\rangle \pm \delta\,|1\rangle$ become parallel as $\delta \to 0$, while the eigenvalue splitting $2E$ remains finite. This eigenstate coalescence at a fixed gap is what distinguishes the protocol from EP-based sensing. At an exceptional point both eigenvalues and eigenvectors coalesce, so that the response is enhanced through the square-root behaviour of the eigenvalue splitting, an enhancement that is generically offset by excess noise and the Petermann factor [34, 35, 38]. Here, by contrast, the eigenvalue gap $2E$ remains finite as $\delta \to 0$, whereas $\partial_\lambda \delta$ becomes large. The sensing response is therefore steep without invoking a spectral singularity. The protocol can be realised by coherently controlling the two-qubit Hermitian dilation introduced below.

B. Two-qubit Hermitian dilation

The non-unitary dynamics generated by Eq. (1) is recovered through the Naimark-dilation construction of Ref. [41], in which the single-qubit pseudo-Hermitian sensor of the bottom row of Fig. 1(a) is obtained by postselecting the two-qubit Hermitian process of the top row. The sensor qubit s is coupled to an ancilla qubit a and evolved under the two-qubit Hermitian Hamiltonian

$$H_{\rm dil}(\lambda) = b_\lambda\, I_a \otimes \sigma_x^{(s)} - c\,\sigma_y^{(a)} \otimes \sigma_y^{(s)}, \tag{2}$$

whose couplings are fixed by a single asymmetry parameter $\varepsilon \ll 1$,

$$b = \frac{4\varepsilon(1+\varepsilon)}{1+2\varepsilon}\,\omega, \qquad c = \frac{2\sqrt{\varepsilon(1+\varepsilon)}}{1+2\varepsilon}\,\omega, \tag{3}$$

with ω an overall energy scale. The dilation is therefore controlled by a single asymmetry parameter ε, together with the dynamical parameter λ to be estimated. The couplings in Eq. (3) are determined by the matching condition that the postselected branch of $H_{\rm dil}$ reproduces H_s of Eq. (1), so b and c are not free parameters of the model.

The sensor and ancilla are prepared in the product state

$$|\Psi(0)\rangle = \big(\alpha\,|0\rangle_a + \beta\,|1\rangle_a\big) \otimes |0\rangle_s, \tag{4}$$

with

$$\alpha^2 = \frac{1+\varepsilon}{1+2\varepsilon}, \qquad \beta^2 = \frac{\varepsilon}{1+2\varepsilon}. \tag{5}$$

After unitary evolution for time t under $H_{\rm dil}$, the two-qubit state $|\Psi(t)\rangle = e^{-iH_{\rm dil}t}|\Psi(0)\rangle$ is projected onto the ancilla outcome $|0\rangle_a$. The conditional dynamics of the sensor in the surviving branch coincides with that generated by the effective Hamiltonian $H_s(E_\lambda, \delta_\lambda)$ of Eq. (1), with

$$E_\lambda = \sqrt{b_\lambda^2 + c^2}, \qquad \delta_\lambda = \frac{\lambda + 2\varepsilon\omega}{E_\lambda}. \tag{6}$$

The parameter λ thus enters both the oscillation scale E_λ and the eigenstate parameter δ_λ. Eigenstate coalescence, $\delta_\lambda = 0$, is reached at

$$\lambda_c = -2\varepsilon\omega, \tag{7}$$

where the eigenvalues $\pm E_{\lambda_c}$ stay split.

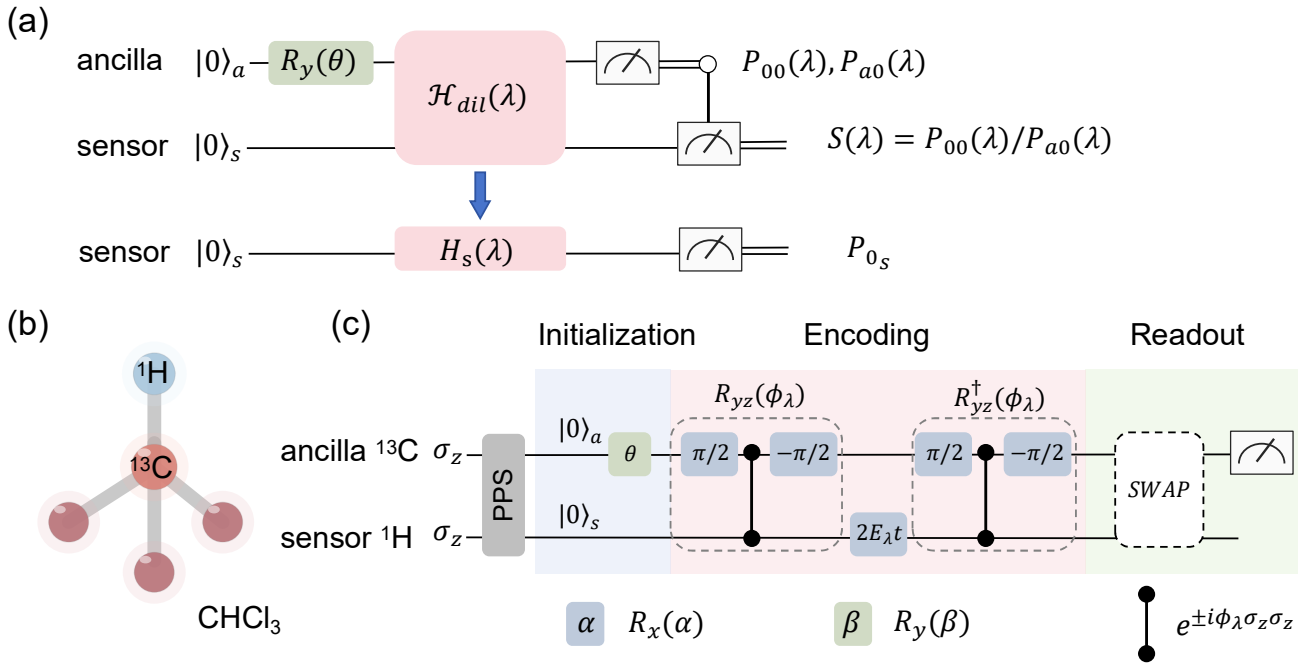


FIG. 1. Pseudo-Hermitian sensing protocol and its NMR realisation. (a) Logical scheme of the Naimark dilation. Top row, two-qubit Hermitian register with ancilla a and sensor s initialised in $|0\rangle$. An ancilla rotation $R_y(\theta)$ with $\theta = 2\arctan\sqrt{\varepsilon/(1+\varepsilon)}$ prepares the input state of Eq. (4), the two-qubit Hermitian Hamiltonian $H_{\rm dil}(\lambda)$ of Eq. (2) encodes the parameter, and population measurements in the computational basis yield the joint probability $P_{00}(\lambda)$ and the ancilla-marginal postselection probability $P_{a0}(\lambda) = P_{00}+P_{01}$. Conditioning the sensor readout on the ancilla outcome $|0\rangle_a$ (open circle) returns the conditional signal $S(\lambda) = P_{00}(\lambda)/P_{a0}(\lambda)$. Bottom row, the corresponding effective single-qubit pseudo-Hermitian evolution $H_s(\lambda)$ of Eq. (1) obtained by Naimark projection on $|0\rangle_a$, whose sensor $|0\rangle$ population satisfies $P_{0_s}(\lambda) = S(\lambda)$. (b) Molecular structure of ^{13}C-labelled chloroform used as the two-qubit register. The ^{13}C nucleus serves as the ancilla and the ^{1}H nucleus as the sensor. (c) Compiled NMR pulse circuit on the same register. The pseudo-pure state of Eq. (20) is prepared by spatial averaging (PPS block) from the thermal Zeeman polarisations σ_z, after which the ancilla rotation $R_y(\theta)$ encodes ε into the input state. The dilated propagator $U_{\rm dil}(\lambda, t)$ follows the three-block decomposition in Eq. (22). Each dashed $R_{YZ}(\phi_\lambda)$ module contains (i) an ancilla rotation $R_x^{(a)}(\pi/2)$, (ii) scalar-coupling evolution $\exp[-i\phi_\lambda \sigma_z^{(a)}\sigma_z^{(s)}/2]$, and (iii) $R_x^{(a)}(-\pi/2)$; the inverse module uses the reversed sequence. The central sensor rotation has angle $2E_\lambda t$. A SWAP between the two spins maps the ^{1}H populations onto ^{13}C so that all readouts are taken on the ^{13}C channel. Coloured boxes denote single-qubit rotations $R_x(\alpha)$ and $R_y(\beta)$. Parameters $\varepsilon = 0.08$, $\omega = 1$, $J \approx 214.6$ Hz.

C. Conditional and absolute probabilities

The two-qubit dynamics generated by $H_{\rm dil}$ admits a simple closed form. Writing $A = I_a \otimes \sigma_x^{(s)}$ and $B = \sigma_y^{(a)} \otimes \sigma_y^{(s)}$, the operators satisfy $A^2 = B^2 = I$ together with $\{A, B\} = 0$, so that $H_{\rm dil}^2 = (b_\lambda^2 + c^2)I = E_\lambda^2 I$. The full two-qubit unitary $e^{-iH_{\rm dil}t}$ therefore oscillates at a single frequency E_λ, identical to the energy scale of the effective sensor in Eq. (6). The directly measurable joint population of the retained outcome $|0\rangle_a|0\rangle_s$ is

$$P_{00}(\lambda, t) = \alpha^2 \cos^2(E_\lambda t), \tag{8}$$

and the probability that the ancilla postselection succeeds is

$$P_{a0}(\lambda, t) = P_{00} + P_{01} = \alpha^2\left[\cos^2(E_\lambda t) + \delta_\lambda^2 \sin^2(E_\lambda t)\right]. \tag{9}$$

The normalised, postselected population of the sensor in $|0\rangle_s$ follows as the ratio

$$S(\lambda, t) = \frac{P_{00}(\lambda, t)}{P_{a0}(\lambda, t)} = \frac{1}{1 + \delta_\lambda^2 \tan^2(E_\lambda t)}. \tag{10}$$

Equation (10) is the pseudo-Hermitian sensing signal of Ref. [41]. At interrogation times for which $\tan^2(E_\lambda t)$ is large, the ratio is controlled by $\delta_\lambda^2 \tan^2(E_\lambda t)$, so that a small change of λ near λ_c drives S from near unity to near zero on a parameter scale set by $\partial_\lambda \delta_\lambda$. This response is much steeper than the cosine-squared fringe of a Ramsey interferometer on the same qubit, and reflects the rapid rotation of the right eigenstates discussed in Sec. II A.

The two observables S and P_{00} play distinct roles in the comparison below. The conditional signal S is defined only on the postselected sub-ensemble, whereas the joint population P_{00} is the absolute probability obtained from the full two-qubit Hermitian process and contains, through $P_{a0} = P_{00}+P_{01}$, the success rate of the postselec-

tion. A single set of computational-basis population measurements yields both observables from the same dataset, as indicated by the joint measurement on the right of Fig. 1(a), so that the amplified conditional response and the cost of producing it are accessed together rather than inferred from independent calibrations.

D. Sensitivity and the resource limit

To compare the conditional and absolute responses on the same statistical basis, we associate a binary outcome probability $q(\lambda)$ with the sensitivity [5]

$$\delta\lambda_q = \frac{\sqrt{q(1-q)}}{|\partial_\lambda q|}. \tag{11}$$

For the two outcomes with probabilities q and $1-q$, the classical Fisher information (CFI) is

$$F_C[q] = \frac{(\partial_\lambda q)^2}{q(1-q)}, \tag{12}$$

so that $\delta\lambda_q = 1/\sqrt{F_C[q]}$. Setting $q = S$ and $q = P_{00}$ gives the conditional sensitivity $\delta\lambda_S$ and the sensitivity $\delta\lambda_{P_{00}}$ obtained from the absolute joint probability, respectively.

These two quantities account for the postselection resource differently. The normalisation in $S = P_{00}/P_{a0}$ removes the probability of obtaining the accepted ancilla outcome, whereas $P_{00} = P_{a0}S$ retains this probability. We therefore use $\delta\lambda_S$ to characterise the conditional response and $\delta\lambda_{P_{00}}$ for the comparison with a Ramsey sensor that includes the postselection cost. The Ramsey sequence uses the same sensor qubit, the same $\lambda\sigma_x^{(s)}$ generator, and the same interrogation time; its sensitivity $\delta\lambda_R$ is evaluated at the point of maximum slope of the fringe.

The sensitivity $\delta\lambda_{P_{00}}$ refers to the binary population measurement implemented in the experiment and does not use the full four-outcome distribution. We therefore also consider the CFI of a complete measurement of both qubits in the computational basis and the quantum Fisher information (QFI), which sets the information bound of the output state independently of the measurement choice. The four probabilities P_{mn} give

$$F_C^{\mathrm{comp}} = \sum_{m,n=0,1} \frac{\left(\partial_\lambda P_{mn}\right)^2}{P_{mn}}. \tag{13}$$

For the ideal state generated by $H_{\mathrm{dil}}(\lambda)$, the QFI is

$$F_Q^{\mathrm{dil}} = 4\left[\frac{x_\lambda^2}{E_\lambda^2}t^2 + \frac{c^2}{E_\lambda^4}\sin^2(E_\lambda t)\right], \qquad x_\lambda = b + \lambda. \tag{14}$$

The phases of the computational-basis amplitudes do not depend on λ, and the parameter dependence of the ideal state is therefore fully contained in the four probabilities. Consequently,

$$F_C^{\mathrm{comp}} = F_Q^{\mathrm{dil}}. \tag{15}$$

Together with $\sin^2(E_\lambda t) \le E_\lambda^2 t^2$, this gives

$$\frac{1}{\delta\lambda_{P_{00}}^2} \le F_C^{\mathrm{comp}} = F_Q^{\mathrm{dil}} \le 4t^2 = F_Q^{\mathrm{R}}, \tag{16}$$

where F_Q^{R} is the optimal Ramsey QFI under the same encoding conditions. This hierarchy separates the information discarded by grouping the four outcomes into the binary event P_{00} from the bound imposed by the ideal two-qubit state. The derivation and numerical comparison are provided in Supplemental Sec. SI and Fig. S1.

III. EXPERIMENT

To test the pseudo-Hermitian response and its postselection cost in one device, we implement the Naimark-dilated sensing protocol of Ref. [41] on a two-spin NMR processor.

A. Sample and control

We use ^{13}C-labelled chloroform dissolved in acetone-d_6 on a Bruker Avance III 600-MHz spectrometer at room temperature. The ^{13}C and ^{1}H nuclear spins encode the ancilla qubit a and the sensor qubit s, respectively [Fig. 1(b)]. In the doubly rotating frame, the internal Hamiltonian of the register is

$$H_{\mathrm{int}} = -\pi \sum_{j=a,s} \nu_j\, \sigma_z^{(j)} + \frac{\pi J}{2}\, \sigma_z^{(a)}\sigma_z^{(s)}, \tag{17}$$

with chemical-shift offsets ν_j and scalar coupling $J \approx 214.6$ Hz. Resonant radio-frequency (RF) pulses applied to the two channels implement rotations of each spin about axes in the transverse plane,

$$H_{\mathrm{rf}}(t) = \frac{1}{2}\sum_{j=a,s} \Omega_j(t)\left[\cos\varphi_j(t)\,\sigma_x^{(j)} + \sin\varphi_j(t)\,\sigma_y^{(j)}\right], \tag{18}$$

where the amplitudes $\Omega_j(t)$ and phases $\varphi_j(t)$ set the rotation angles and axes. Together with the native ZZ coupling of Eq. (17), $H_{\mathrm{int}} + H_{\mathrm{rf}}(t)$ supplies the universal control resource of the platform.

Throughout the experiment $\varepsilon = 0.08$ and $\omega = 1$, which give $b \simeq 0.298$ and $c \simeq 0.507$ from Eq. (3). The dimensionless model frequencies are mapped to NMR control frequencies by an overall scaling factor

$$k = \frac{2\pi J}{c}, \tag{19}$$

fixed by matching c to the physical scalar coupling $2\pi J$. Under this mapping, the model offset b_λ corresponds to an NMR detuning $kb_\lambda/(2\pi)$, and the model interrogation time t is mapped to $t_{\mathrm{phys}} = t/k = ct/(2\pi J)$. For the interrogation time used in the experiment, $t = \pi/[4\omega\sqrt{\varepsilon(1+\varepsilon)}]$, this gives $t_{\mathrm{phys}} \simeq 1.00$ ms.

The implemented value $\varepsilon = 0.08$ balances the width of the conditional response against the absolute population available for readout. A theoretical scan over $0.02 \leq \varepsilon \leq 0.20$, presented in Supplemental Sec. SII and Fig. S2, shows that reducing ε narrows the peak of $S(\lambda)$ while lowering P_{00} in the relevant parameter range, whereas increasing ε broadens the response and raises the absolute population. The choice $\varepsilon = 0.08$ therefore retains a resolvable pseudo-Hermitian response together with a measurable absolute signal.

B. Initialisation, evolution, and readout

The register is initialised to the pseudo-pure state (PPS) $|00\rangle$ from thermal equilibrium by spatial averaging [45, 46]. In NMR deviation density-matrix notation, this preparation converts the thermal magnetisation $\rho_{\rm th}^{\rm dev} \propto \gamma_C \sigma_z^{(a)} + \gamma_H \sigma_z^{(s)}$ into

$$\rho_{\rm PPS}^{\rm dev} \propto \sigma_z^{(a)} + \sigma_z^{(s)} + \sigma_z^{(a)}\sigma_z^{(s)}, \tag{20}$$

which corresponds to $|00\rangle\langle 00|$ up to an unobservable identity component invariant under the subsequent unitaries. The spatial-averaging sequence combines calibrated RF rotations with pulsed field gradients to redistribute the diagonal populations and dephase unwanted coherences.

An ancilla rotation $R_y(\theta)$ with

$$\theta = 2\arctan\sqrt{\frac{\varepsilon}{1+\varepsilon}} \tag{21}$$

prepares the input state of Eq. (4), after which the dilated propagator $U_{\rm dil}(\lambda, t) = \exp[-iH_{\rm dil}(\lambda)t]$ encodes λ. To implement $U_{\rm dil}$ on the present register, we use the exact decomposition

$$U_{\rm dil}(\lambda, t) = R_{YZ}(\phi_\lambda)\, R_x^{(s)}(2E_\lambda t)\, R_{YZ}^\dagger(\phi_\lambda), \tag{22}$$

where $\cos\phi_\lambda = b_\lambda/E_\lambda$, $\sin\phi_\lambda = c/E_\lambda$, and $R_{YZ}(\phi) = \exp[+i\phi\, \sigma_y^{(a)} \otimes \sigma_z^{(s)}/2]$. Equation (22) follows from $\{I \otimes \sigma_x, \sigma_y \otimes \sigma_y\} = 0$, which gives $H_{\rm dil}^2 = E_\lambda^2 I$ and turns $U_{\rm dil}$ into a single-qubit x rotation of the sensor by angle $2E_\lambda t$ in the basis tilted by R_{YZ}. The central rotation $R_x^{(s)}(2E_\lambda t)$ is generated by RF control on the ^{1}H channel, while R_{YZ} is generated by enclosing a scalar-coupling evolution between $\pi/2$ rotations on the ancilla,

$$R_{YZ}(\phi_\lambda) = R_x^{(a)}\!\left(\tfrac{\pi}{2}\right) \exp\!\left(-i\tfrac{\phi_\lambda}{2}\, \sigma_z^{(a)}\sigma_z^{(s)}\right) R_x^{(a)}\!\left(-\tfrac{\pi}{2}\right), \tag{23}$$

with the central scalar-coupling interval $\tau_\lambda = \phi_\lambda/(\pi J)$ before compilation. The full compiled sequence is shown in Fig. 1(c).

Readout uses two acquisitions on the ^{13}C channel. The first reads the ^{13}C diagonal directly, and the second is preceded by a SWAP between the two spins so that the ^{1}H populations are mapped onto ^{13}C before detection when needed. Combining the two acquisitions gives the required diagonal elements $P_{mn} = \langle mn|\rho|mn\rangle$, from which P_{00}, P_{a0}, and S are formed as defined in Sec. II. A common readout normalisation calibrated from reference measurements multiplies P_{mn} and cancels in the ratio $S = P_{00}/P_{a0}$.

The input-state preparation $R_y(\theta)$, the dilated propagator $U_{\rm dil}(\lambda, t)$, and the readout-axis rotation are implemented as shaped RF pulses optimised by gradient ascent pulse engineering (GRAPE) [48], with simulated fidelities exceeding 0.999 against the target unitaries. The total duration of the shaped RF control pulses is approximately 9 ms for the direct readout sequence and 16 ms for the sequence in which an additional SWAP operation is applied before acquisition. The relevant coherence times are provided in Supplemental Sec. SIII.

The Hermitian Ramsey benchmark [49, 50] is implemented on the same sensor qubit with the same $\lambda\sigma_x^{(s)}$ encoding as the dilated protocol, so that $\delta\lambda_{P_{00}}$ and $\delta\lambda_R$ are compared at a common encoding convention. The measured Ramsey fringe is fitted to its sinusoidal form, and $\delta\lambda_R$ is evaluated at the maximum-slope working point, where the Ramsey sensitivity is optimal and the error-propagation estimate remains well conditioned.

IV. RESULTS

The conditional signal $S = P_{00}/P_{a0}$ tests whether the postselected branch reproduces the pseudo-Hermitian response of Eq. (10), while the absolute joint probability P_{00} retains the probability scale of the two-qubit dilation and so preserves the resource accounting of Ref. [42]. From these data we extract the susceptibility $\partial_\lambda S$ and the sensitivity $\delta\lambda_{P_{00}}$ obtained from the joint two-qubit probability, the latter being compared with a Ramsey benchmark $\delta\lambda_R$ measured on the same sensor qubit. The sensor is scanned at 25 uniformly spaced values of $\lambda/(\varepsilon\omega) \in [-4, 0]$, a window that brackets the eigenstate-coalescence point $\lambda_c = -2\varepsilon\omega$ on both sides and resolves the pseudo-Hermitian peak of Eq. (10) together with its rapid decrease as λ approaches zero. At each scan point, the population-readout procedure described in Sec. III gives the diagonal populations $P_{mn} = \langle mn|\rho|mn\rangle$. The quantities P_{00}, $P_{a0} = P_{00} + P_{01}$, and $S = P_{00}/P_{a0}$ are then formed as in Sec. II. The Ramsey sequence on the same sensor qubit, processed identically, fixes the Hermitian benchmark $\delta\lambda_R$. A parallel dataset acquired with a finite-difference shift $\Delta\lambda = \lambda/5$ provides the susceptibilities $\partial_\lambda S$ and $\partial_\lambda P_{00}$ used in the sensitivity analysis below. (We reserve the symbol $\delta\lambda$ for sensitivities $\delta\lambda_q$ and use $\Delta\lambda$ for the finite-difference step.)

A. Probability response

The measured $P_{00}(\lambda)$ is shown in Fig. 2(b) together with the theoretical prediction of Eq. (8). Across the scanned range, the data reproduce the overall cosine-squared dependence at the sensor energy E_λ, includ-

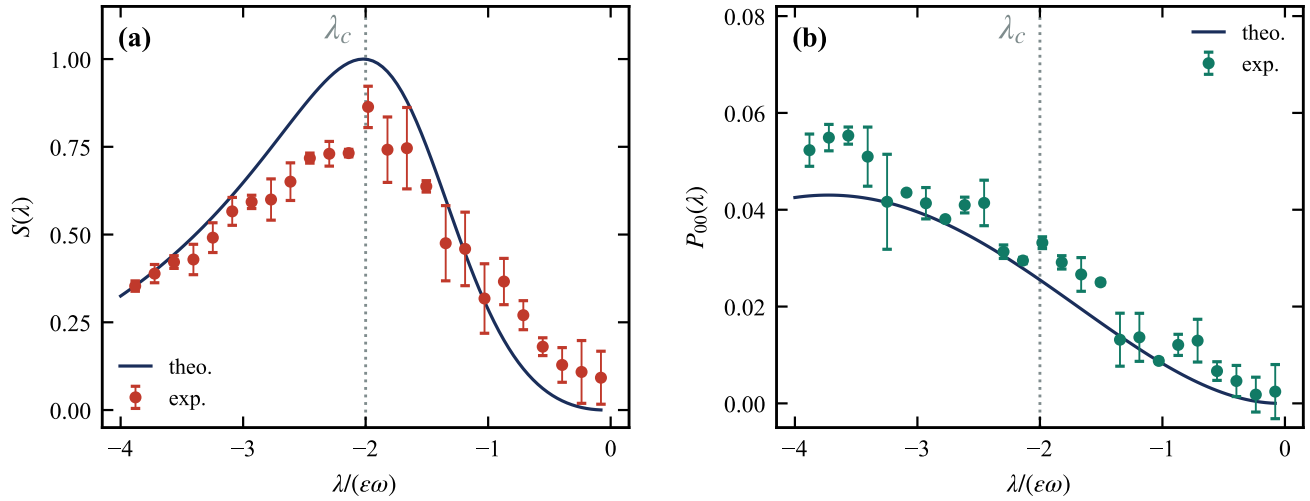


FIG. 2. Measured conditional signal $S(\lambda)$ (a, red) and two-qubit probability $P_{00}(\lambda)$ (b, teal) versus $\lambda/(\varepsilon\omega)$ in the scanned range $[-4, 0]$. Solid navy lines, theoretical predictions of Eqs. (10) and (8). Markers and error bars, mean values and standard errors of the mean obtained from independent repeated scans. The vertical dotted line marks the coalescence point $\lambda_c = -2\varepsilon\omega$. Parameters $\varepsilon = 0.08$, $\omega = 1$.

ing the shallow minimum below the coalescence point $\lambda_c = -2\varepsilon\omega$. Residual deviations from the ideal curve may arise from decoherence and residual errors in control and population reconstruction.

The influence of these deviations is enhanced by the small absolute scale of P_{00}. Inside the working window $\lambda/(\varepsilon\omega) \in [-1, -0.4]$ used for the sensitivity analysis below, P_{00} ranges from a few 10^{-3} to a few 10^{-2}. The small scale is set primarily by the $\cos^2(E_\lambda t)$ factor at the chosen interrogation time, while the prefactor $\alpha^2 = (1+\varepsilon)/(1+2\varepsilon) \simeq 0.93$ provides only an overall rescaling. Consequently, small absolute deviations in the reconstructed populations can produce appreciable relative changes in P_{00} and its finite-difference derivative.

The measured $S(\lambda)$ in Fig. 2(a) reproduces the predicted pseudo-Hermitian response, reaching a maximum of approximately 0.85 near λ_c and decreasing sharply as λ approaches zero. In the ideal model, $P_{01} = 0$ at λ_c, so that $S = 1$. The experimental value below unity reflects a residual P_{01} contribution, whose relative influence is enhanced by the conditional normalisation. The Pearson linear correlation coefficients between experiment and theory over the analysed range are $r = 0.985$ for $S(\lambda)$ and $r = 0.978$ for $P_{00}(\lambda)$.

B. Susceptibility and sensitivity comparison

The error-propagation expression in Eq. (11) depends on the slope $\partial_\lambda q$, so that a reliable analysis requires stable finite-difference estimates of $\partial_\lambda S$ and $\partial_\lambda P_{00}$. Two practical choices control this step. First, the finite-difference shift $\Delta\lambda = \lambda/5$ introduced above is chosen large enough that the signal change exceeds the noise floor of the population estimate, and small enough that the linearisation $\partial_\lambda q \simeq [q(\lambda + \Delta\lambda) - q(\lambda)]/\Delta\lambda$ remains accurate across the rapidly varying region near λ_c. Second, the averaged $S(\lambda)$ and $P_{00}(\lambda)$ are lightly smoothed by a nine-point local quadratic Savitzky–Golay fit [51] before differentiation, so that high-frequency fluctuations introduced by the differencing are removed without distorting the underlying parameter dependence. The unsmoothed averaged means are retained for the $S(\lambda)$ and $P_{00}(\lambda)$ plots, so that smoothing affects only the derived sensitivity figures.

Figure 3(a) shows the resulting susceptibility $\partial_\lambda S$. The slope is positive below λ_c, crosses zero at the peak of $S(\lambda)$, and becomes large and negative just above. The experimental susceptibility reproduces this structure with Pearson correlation $r = 0.92$. The agreement shows that the population data also reproduce the derivative structure of the conditional response.

Figure 3(b) compares the sensitivity $\delta\lambda_{P_{00}}$ with the Ramsey benchmark $\delta\lambda_R \simeq 0.10\,\varepsilon\omega$ extracted from the maximum-slope working point of the Ramsey fringe. The experimental values of $\delta\lambda_{P_{00}}$ are obtained by substituting the measured P_{00} and its finite-difference derivative into Eq. (11). The theoretical $\delta\lambda_{P_{00}}$ remains above the Ramsey benchmark throughout the plotted range, and the experimental data follow the same trend within the reliable working window, consistent with the resource bound of Refs. [42, 43].

V. DISCUSSION

The results above complement the photonic demonstration of Xiao *et al.* [44], and the two experiments realise distinct routes to pseudo-Hermitian sensing without exceptional points. In the lossy single-qubit route, the

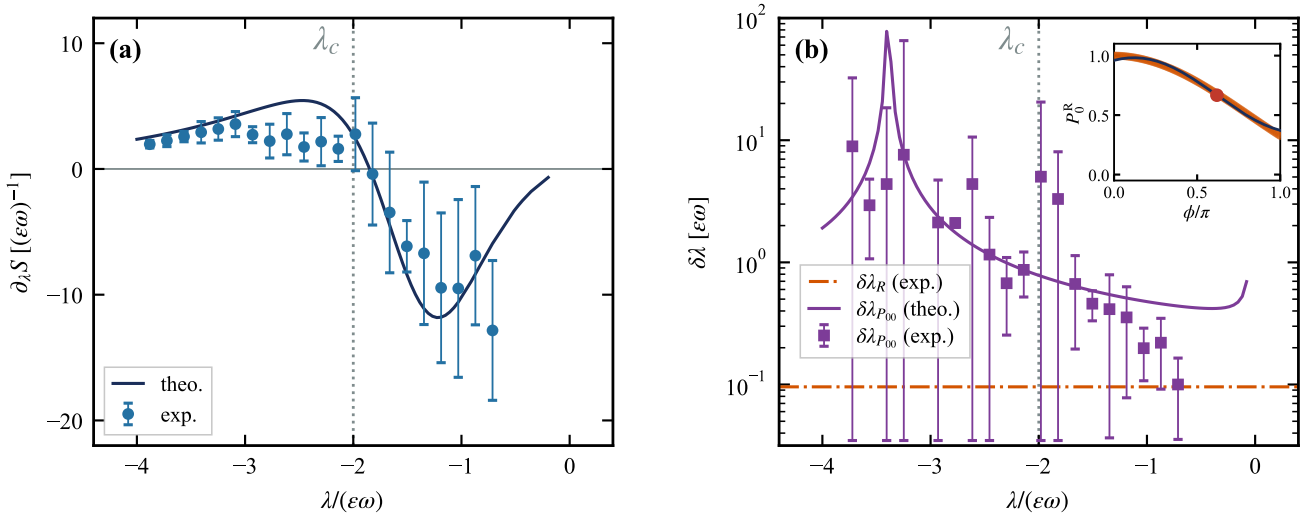


FIG. 3. (a) Finite-difference susceptibility $\partial_\lambda S$ versus $\lambda/(\varepsilon\omega)$. Navy solid line, theory. Blue circles with error bars, experimental data with uncertainties propagated from the repeated measurements through the finite-difference derivative. The vertical dotted line marks the coalescence point $\lambda_c = -2\varepsilon\omega$. (b) Sensitivity $\delta\lambda_{P_{00}}$ on a logarithmic scale, compared with the Hermitian Ramsey benchmark. Solid line, theoretical $\delta\lambda_{P_{00}}$ (purple). Squares, experimental $\delta\lambda_{P_{00}}$. Dash-dotted line, Ramsey benchmark $\delta\lambda_R$ (orange) taken at the maximum-slope working point of the Ramsey fringe, which serves as the Hermitian reference for the comparison with $\delta\lambda_{P_{00}}$. Portions of the error bars extending below the plotted log range are clipped by the axis. Inset, the measured Ramsey fringe $P_0^{\mathrm{R}}(\phi)$ from which $\delta\lambda_R$ is extracted (orange markers), with the sinusoidal fit (navy line) and the maximum-slope working point at which the benchmark is evaluated (red marker). Parameters $\varepsilon = 0.08$, $\omega = 1$.

photonic probe evolves under genuinely non-unitary dynamics, for which the non-Hermitian Hamiltonian is the natural effective description. There is no ancilla or postselection, and hence no separate postselection probability in the resource budget. In the dilation route considered here, the two-qubit register evolves coherently under a Hermitian Hamiltonian, and the pseudo-Hermitian sensor appears as a postselected branch. Both routes exploit the rapid parameter dependence associated with pseudo-Hermitian eigenstate coalescence, but they differ in their physical implementation and resource accounting.

Accurate reconstruction of small populations remains the main experimental challenge in the dilation route, because the sensitivity estimate depends on the finite-difference derivative of P_{00}.

VI. CONCLUSION

By resolving the complete two-qubit population distribution, our experiment places the conditional pseudo-Hermitian response and its postselection cost on the same experimental footing. The sharp response near eigenstate coalescence is recovered, but the sensitivity inferred from the absolute probability P_{00} does not improve upon the Ramsey benchmark in the analysed range, consistent with the ideal-state resource bound. These branch-resolved population measurements provide a direct way to evaluate postselected sensing protocols with explicit resource accounting.

ACKNOWLEDGMENTS

Project supported by the National Natural Science Foundation of China (Grant Nos. 12275117 and 92576109), the Guangdong Basic and Applied Basic Research Foundation (Grant No. 2022B1515020074), and the Shenzhen Science and Technology Program (Grant No. QNXMB20250701092309013).

[1] Helstrom C W 1969 *J. Stat. Phys.* **1** 231–252
[2] Braunstein S L and Caves C M 1994 *Phys. Rev. Lett.* **72** 3439–3443
[3] Giovannetti V, Lloyd S and Maccone L 2006 *Phys. Rev. Lett.* **96** 010401
[4] Giovannetti V, Lloyd S and Maccone L 2011 *Nat. Photon.* **5** 222–229
[5] Degen C L, Reinhard F and Cappellaro P 2017 *Rev. Mod. Phys.* **89** 035002
[6] Pezzè L, Smerzi A, Oberthaler M K, Schmied R and Treutlein P 2018 *Rev. Mod. Phys.* **90** 035005
[7] Long Z and Pang S 2025 *Chin. Phys. B* **34** 080301
[8] Yang B J 2026 *Chin. Phys. Lett.* **43** 020712

[9] Bender C M and Boettcher S 1998 *Phys. Rev. Lett.* **80** 5243–5246
[10] Bender C M 2007 *Rep. Prog. Phys.* **70** 947–1018
[11] Mostafazadeh A 2002 *J. Math. Phys.* **43** 205–214
[12] Mostafazadeh A 2002 *J. Math. Phys.* **43** 2814–2816
[13] El-Ganainy R, Makris K G, Khajavikhan M, Musslimani Z H, Rotter S and Christodoulides D N 2018 *Nat. Phys.* **14** 11–19
[14] Feng L, El-Ganainy R and Ge L 2017 *Nat. Photon.* **11** 752–762
[15] Özdemir S K, Rotter S, Nori F and Yang L 2019 *Nat. Mater.* **18** 783–798
[16] Miri M A and Alù A 2019 *Science* **363** eaar7709
[17] Ashida Y, Gong Z and Ueda M 2020 *Adv. Phys.* **69** 249–435
[18] Bergholtz E J, Budich J C and Kunst F K 2021 *Rev. Mod. Phys.* **93** 015005
[19] Heiss W D 2012 *J. Phys. A: Math. Theor.* **45** 444016
[20] Berry M V 2004 *Czech. J. Phys.* **54** 1039–1047
[21] Wiersig J 2014 *Phys. Rev. Lett.* **112** 203901
[22] Wiersig J 2016 *Phys. Rev. A* **93** 033809
[23] Liu Z P, Zhang J, Özdemir S K, Peng B, Jing H, Lü X Y, Li C W, Yang L, Nori F and Liu Y X 2016 *Phys. Rev. Lett.* **117** 110802
[24] Chen W, Özdemir S K, Zhao G, Wiersig J and Yang L 2017 *Nature* **548** 192–196
[25] Hodaei H, Hassan A U, Wittek S, Garcia-Gracia H, El-Ganainy R, Christodoulides D N and Khajavikhan M 2017 *Nature* **548** 187–191
[26] Lai Y H, Lu Y K, Suh M G, Yuan Z and Vahala K 2019 *Nature* **576** 65–69
[27] Hokmabadi M P, Schumer A, Christodoulides D N and Khajavikhan M 2019 *Nature* **576** 70–74
[28] Wang H, Lai Y H, Yuan Z, Suh M G and Vahala K 2020 *Nat. Commun.* **11** 1610
[29] Kononchuk R, Cai J, Ellis F M, Thevamaran R and Kottos T 2022 *Nature* **607** 697–702
[30] Naghiloo M, Abbasi M, Joglekar Y N and Murch K W 2019 *Nat. Phys.* **15** 1232–1236
[31] Yu S, Meng Y, Tang J S, Xu X Y, Wang Y T, Yin P, Ke Z J, Liu W, Li Z P, Yang Y Z *et al.* 2020 *Phys. Rev. Lett.* **125** 240506
[32] Ding L, Shi K, Zhang Q, Shen D, Zhang X and Zhang W 2021 *Phys. Rev. Lett.* **126** 083604
[33] Hou X, Deng F, Han Z, Ma Y, Wang C, Li Y, Cheng K, Ma K, Shao Y, Zhou R, Zhang Y, Liu M and Zhang H 2026 *Chin. Phys. B* **35** 057802
[34] Langbein W 2018 *Phys. Rev. A* **98** 023805
[35] Lau H K and Clerk A A 2018 *Nat. Commun.* **9** 4320
[36] Zhang M, Sweeney W R, Hsu C W, Yang L, Stone A D and Jiang L 2019 *Phys. Rev. Lett.* **123** 180501
[37] Chen C, Jin L and Liu R B 2019 *New J. Phys.* **21** 083002
[38] Wiersig J 2020 *Photon. Res.* **8** 1457–1467
[39] Duggan R, Mann S A and Alu A 2022 *ACS Photonics* **9** 1554–1566
[40] Loughlin H and Sudhir V 2024 *Phys. Rev. Lett.* **132** 243601
[41] Chu Y, Liu Y, Liu H and Cai J 2020 *Phys. Rev. Lett.* **124** 020501
[42] Ding W, Wang X and Chen S 2023 *Phys. Rev. Lett.* **131** 160801
[43] Zeng N, Liu T, Xia K, Zhang Y R and Nori F 2025 *Phys. Rev. Research* **7** 043219
[44] Xiao L, Chu Y, Lin Q, Lin H, Yi W, Cai J and Xue P 2024 *Phys. Rev. Lett.* **133** 180801
[45] Cory D G, Fahmy A F and Havel T F 1997 *Proc. Natl. Acad. Sci. USA* **94** 1634–1639
[46] Gershenfeld N A and Chuang I L 1997 *Science* **275** 350–356
[47] Vandersypen L M K and Chuang I L 2005 *Rev. Mod. Phys.* **76** 1037–1069
[48] Khaneja N, Reiss T, Kehlet C, Schulte-Herbrüggen T and Glaser S J 2005 *J. Magn. Reson.* **172** 296–305
[49] Ramsey N F 1950 *Phys. Rev.* **78** 695–699
[50] Bollinger J J, Itano W M, Wineland D J and Heinzen D J 1996 *Phys. Rev. A* **54** R4649–R4652
[51] Savitzky A and Golay M J E 1964 *Anal. Chem.* **36** 1627–1639